
Linear combinations of latents in diffusion models: interpolation and beyond

Erik Bodin
University of Cambridge
sepb2@cam.ac.uk

Henry Moss
University of Cambridge
hm493@cam.ac.uk

Carl Henrik Ek
University of Cambridge
che29@cam.ac.uk

Abstract

Generative models are crucial for applications like data synthesis and augmentation. Diffusion, Flow Matching and Continuous Normalizing Flows have shown effectiveness across various modalities, and rely on Gaussian latent variables for generation. As any generated object is directly associated with a particular latent variable, we can manipulate the variables to exert control over the generation process. However, standard approaches for combining latent variables, such as spherical interpolation, only apply or work well in special cases. Moreover, current methods for obtaining low-dimensional representations of the data, important for e.g. surrogate models for search and creative applications, are network and data modality specific. In this work we show that the standard methods to combine variables do not yield intermediates following the distribution the models are trained to expect. We propose Combination of Gaussian variables (COG), a novel interpolation method that addresses this, is easy to implement yet matches or improves upon current methods. COG addresses linear combinations in general and, as we demonstrate, also supports other operations including e.g. defining subspaces of the latent space, simplifying the creation of expressive low-dimensional spaces of high-dimensional objects using generative models based on Gaussian latents.

1 Introduction

Generative models are a cornerstone of machine learning, with diverse applications including image synthesis, data augmentation, and creative content generation. Diffusion models Ho et al. (2020); Song et al. (2020a,b) have emerged as a particularly effective approach to generative modeling for various modalities, such as for images Ho et al. (2020), audio Kong et al. (2020), video Ho et al. (2022), and 3D models Luo & Hu (2021). A yet more recent approach to generative modelling is Flow Matching (FM) Lipman et al. (2022), built upon Continuous Normalizing Flows Chen et al. (2018), generalising the diffusion approach to allow for different probability paths between data distribution and noise distributions, e.g. through Optimal Transport Gulrajani et al. (2017); Villani et al. (2009). All these models allow an invertible connection between latent space and data space.

Diffusion and FM models are trained over the index range of a gradual transformation of data such that at the final step the transformed data is drawn from a predetermined (typically unit) Gaussian. New data can then be generated by sampling from the predetermined distribution followed by using the trained network to run the procedure backwards. As demonstrated by Song et al. (2020a,b); Luo & Hu (2021), semantically meaningful interpolation of high-dimensional objects, e.g. images, can be achieved by defining an appropriate interpolation between their corresponding latent vectors. As simple linear interpolation often works poorly in practice — the intermediate norms for linear interpolation are extremely unlikely for (unit) Gaussian vectors (see White (2016) and Samuel et al. (2024) for a discussion) — the prevailing method is instead spherical interpolation Shoemake (1985). More recently, Samuel et al. (2024) propose a metric and a sophisticated Norm-Aware Optimization

procedure which favours interpolation paths and centroids with likely norms. However, their approach requires numerical optimization of the noise vectors which is expensive in relation to closed-form expressions, often yields worse results than simpler methods, and is not applicable to general linear combinations including the subspace projections that are the primary focus of this work. In Kwon et al. (2022); Haas et al. (2023) it was shown that composable image editing directions can be recovered from a UNet Ronneberger et al. (2015) denoiser network. However, the methods require modifications to the generative procedure, introduces extra computation, and are specific to UNet-based models.

In this work, we demonstrate that effective interpolation can be achieved by adhering to a core assumption of the generative process; that the latent variables follow the distribution the generative process assumes and the network has been trained on. Starting with Gaussian-distributed latent variables, we introduce Combination of Gaussian variables (COG) — a simple scheme for ensuring that interpolation intermediates match the latents’ distribution. Our proposed scheme applies to general linear combinations such as addition, centroid calculation and subspace projections, is easy to implement through a closed-form expression, and is shown to outperform or match state-of-the-art baselines. We demonstrate that we can form meaningful low-dimensional spaces of high-dimensional objects using both diffusion models and flow matching models without making assumptions about the network or data modality.



Figure 1: **Centroid determination.** The centroid of the latents x_1 , x_2 , x_3 as determined using the different methods, with the result shown in the respective (right-most) plot. We note that using COG instead of the other methods gets rid of several artifacts, such as the unrealistic headlights and chassis texture. The diffusion model Stable Diffusion 2.1 Rombach et al. (2022) is used in this example.



Figure 2: **Low-dimensional subspaces.** The latents x_1, \dots, x_5 (corresponding to images) are converted into basis vectors and used to define a 5-dimensional subspace. The grids show generations from uniform grid points in the subspace coordinate system, where the grids are for the dimensions $\{1, 3\}$ and $\{2, 4\}$, respectively, centered around the coordinate for x_1 . Each coordinate in the subspace correspond to a linear combination of the basis vectors. The flow-matching model Stable Diffusion 3 Esser et al. (2024) is used here. See Section E for more slices of the space and examples.

2 Methodology

As is typical in the generative modelling literature, we assume that the latent variables that initiate the generative process follow a prespecified Gaussian distribution. Therefore all such latents, including ones formed from linear combinations of latents, such as interpolants, centroids and subspace projections, must adhere to this assumption, as this is what the model has been trained to expect. We will now propose a novel method to ensure that any linear combinations of these latents are guaranteed to be valid samples given that the original latents are, to ensure their compatibility with the model. Note that, as described in Nalisnick et al. (2019) (See Appendix F for more details), a high-dimensional vector merely having a high likelihood under the distribution is not sufficient as it may still not have the characteristics of a sample; here we assume the latents have either been explicitly sampled from the distribution or obtained through accurate generation inversion.

Consider latents $\mathbf{x}^{(i)} \in \mathbb{R}^D$, i.e random variables following the predetermined Gaussian distribution $\mathcal{N}(\boldsymbol{\mu}, \boldsymbol{\Sigma})$ at the initial step of the generative process. Further, let \mathbf{y} be a linear combination of K i.i.d. latents,

$$\mathbf{y} := \sum_{k=1}^K w_k \mathbf{x}^{(k)} = \mathbf{w}^T \mathbf{X}, \quad (1)$$

where $w_k \in \mathbb{R}$, $\mathbf{w} = [w_1, w_2, \dots, w_K]$ and $\mathbf{X} = [\mathbf{x}^{(1)}, \mathbf{x}^{(2)}, \dots, \mathbf{x}^{(K)}]$. Then we have that \mathbf{y} is also a Gaussian random variable, with mean and covariance

$$\mathbf{y} \sim \mathcal{N}(\alpha \boldsymbol{\mu}, \beta \boldsymbol{\Sigma}) \quad \alpha = \sum_{k=1}^K w_k \quad \beta = \sum_{k=1}^K w_k^2. \quad (2)$$

In other words, \mathbf{y} is only distributed as $\mathcal{N}(\boldsymbol{\mu}, \boldsymbol{\Sigma})$ in the limited special case where (a) $\alpha \boldsymbol{\mu} = \boldsymbol{\mu}$ and (b) $\beta \boldsymbol{\Sigma} = \boldsymbol{\Sigma}$, which is restrictive. For example, using linear interpolation where $\mathbf{w} = [v, 1-v]$, $v \in [0, 1]$, (b) holds only for the endpoints, $v = \{0, 1\}$; for all other values of v the random variable \mathbf{y} *does not* follow the correct distribution $\mathcal{N}(\boldsymbol{\mu}, \boldsymbol{\Sigma})$, which is consistent with that latents away from the endpoints does not lead to valid generations empirically (see Figure 6). Spherical linear interpolation is popular since it is known to work well empirically, and we note that in the popular special case of unit Gaussian latents it is *nearly met*; as $\boldsymbol{\mu} = \mathbf{0}$ in that case, it follows that (a) $\alpha \boldsymbol{\mu} = \boldsymbol{\mu}$, and moreover, (b) β is near 1 for the whole interval $v \in [0, 1]$ for this operation given that \mathbf{x}_1 and \mathbf{x}_2 are independent samples from $\mathcal{N}(\mathbf{0}, \mathbf{I})$ and the dimensionality D is large. See proof in Appendix B.

In this work, we propose directly transforming linear combinations such that $\alpha = \beta = 1$, for any $\mathbf{w} \in \mathbb{R}^K$, thus **exactly meeting the criteria** for **any** linear combination and **any** choice of $\boldsymbol{\mu}$ and $\boldsymbol{\Sigma}$. We use a linear transformation of the linear combination. That is, we define a transformed random variable substituting the latent linear combination \mathbf{y}

$$\mathbf{z} = \mathbf{a} + \mathbf{B}\mathbf{y} \quad \mathbf{a} = (1 - \frac{\alpha}{\sqrt{\beta}})\boldsymbol{\mu} \quad \mathbf{B} = \frac{1}{\sqrt{\beta}}\mathbf{I} \quad (3)$$

for which it holds that $\mathbf{z} \sim \mathcal{N}(\boldsymbol{\mu}, \boldsymbol{\Sigma})$ given i.i.d. latents $\mathbf{x}^{(i)} \sim \mathcal{N}(\boldsymbol{\mu}, \boldsymbol{\Sigma})$. See Section A for the derivations of Equation 2 and 3. The weights \mathbf{w} , specifying the transformed linear combination \mathbf{z} together with the set of K original latents, depend on the operation. Below are a few examples of popular linear combinations to form \mathbf{y} ; these are used as above to, for the corresponding weights \mathbf{w} , obtain \mathbf{z} following the distribution expected by the generative model.

- **Interpolation:** $\mathbf{y} = v\mathbf{x}_1 + (1-v)\mathbf{x}_2$, where $\mathbf{w} = [v, 1-v]$ and $v \in [0, 1]$.
- **Centroid Determination:** $\mathbf{y} = \frac{1}{K} \sum_{k=1}^K \mathbf{x}_k = \sum_{k=1}^K \frac{1}{K} \mathbf{x}_k$, where $\mathbf{w} = [\frac{1}{K}]^K$.
- **Subspace Projection:** Suppose we wish to build a navigable subspace spanned by linear combinations of K latent variables. By performing the QR decomposition of $\mathbf{A} := [\mathbf{x}_1, \mathbf{x}_2, \dots, \mathbf{x}_K] \in \mathbb{R}^{D \times K}$ to produce a semi-orthonormal matrix $\mathbf{U} \in \mathbb{R}^{D \times K}$ (as the Q-matrix), we can then define a subspace projection of any new \mathbf{x} into the desired subspace via $s(\mathbf{x}) := \mathbf{U}\mathbf{U}^T \mathbf{x} = \mathbf{U}\mathbf{h} \in \mathbb{R}^D$. The weights \mathbf{w} for a given point in the subspace $s(\mathbf{x})$ are given by $\mathbf{w} = \mathbf{A}_\dagger s(\mathbf{x}) = \mathbf{A}_\dagger \mathbf{U}\mathbf{h} \in \mathbb{R}^K$ where \mathbf{A}_\dagger is the Moore–Penrose inverse of \mathbf{A} . See the derivation of the weights and proof in Appendix C. One can directly pick coordinates $\mathbf{h} \in \mathbb{R}^K$ and convert to (yet uncorrected) subspace latents by $\mathbf{y} = \mathbf{U}\mathbf{h}$, which are subsequently used in Equation 3. In Figure 2 we use grids in \mathbb{R}^K to set \mathbf{h} .

3 Experiments

In this section we first assess our proposed linear transformation scheme experimentally, where we perform qualitative and quantitative comparisons to the respective baselines for interpolation and centroid determination. We then demonstrate several examples of low-dimensional subspaces on a popular diffusion and flow-matching model, respectively.

Linear interpolation and centroid determination For the application of interpolation, we compare to linear interpolation (LERP), spherical linear interpolation (SLERP), and Norm-Aware Optimization (NAO) Samuel et al. (2024).

In contrast to the other approaches which only involve analytical expressions, NAO involves a numerical optimization scheme based on a discretization of a line integral. We closely follow the evaluation protocol in Samuel et al. (2024), basing the experiments on Stable Diffusion (SD) 2.1 Rombach et al. (2022) and inversions of random images from 50 random classes from ImageNet1k Deng et al. (2009), and assess visual quality and preservation of semantics using FID scores and class prediction accuracy, respectively. For the interpolation we (randomly without replacement) pair the 50 images per class into 25 pairs, forming 1250 image pairs in total.

Interpolation			
Method	Accuracy	FID	Time
LERP	3.92%	199	$6e^{-3}$ s
SLERP	64.6%	42.6	$9e^{-3}$ s
NAO	62.1%	46.0	30s
COG (ours)	67.4%	38.9	$6e^{-3}$ s
Centroid determination			
Method	Accuracy	FID	Time
Euclidean	0.286%	310	$4e^{-4}$ s
Standardized Euclidean	44.6%	88.8	$1e^{-3}$ s
Mode norm Euclidean	44.6%	88.4	$1e^{-3}$ s
NAO	44.0%	93.0	90s
COG (ours)	46.3%	87.7	$6e^{-4}$ s

Table 1: Quantitative comparisons of baselines.

For the centroid determination we compare to NAO, the Euclidean centroid $\bar{x} = \frac{1}{K} \sum_{k=1}^K x_k$ and two transformations thereof; "standardized Euclidean", where \bar{x} is subsequently standardized to have mean zero and unit variance (as SD 2.1 assumes), and "mode norm Euclidean", where \bar{x} is rescaled for its norm to equal the (square root of the) mode of $\chi^2(D)$, the chi-squared distribution with D degrees of freedom, which is the maximum likelihood norm given that x has been generated from a unit Gaussian with D dimensions. For each class, we form 10 3-groups, 10 5-groups, 4 10-group and 1 25-group, sampled without replacement per group, for a total of 1250 centroids per method. For more details on the experiment setup and settings, see Section D in the appendix.

In Table 1 we show that our method outperforms the baselines in terms of FID scores and accuracy, as calculated using a pre-trained classifier following the evaluation methodology of Samuel et al. (2024). For an illustration of centroids and interpolations see Figure 1 and Figure 13, respectively. The evaluation time of an interpolation path and centroid, shown with one digit of precision, illustrate that the analytical expressions are significantly faster than NAO. Surprisingly, NAO did not perform as well as spherical interpolation and several other baselines, despite that we used their implementation and it was outperforming these methods in Samuel et al. (2024). We note that one discrepancy is that we report FID scores using the standard number of features (2048), while in their paper they are using fewer (64), which in Seitzer (2020) is not recommended since it does not necessarily correlate with visual quality. In the appendix we include results using FID scores using all settings of features. We note that, in our setup, the baselines performs substantially better than reported in their setup - including NAO in terms of FID scores using the 64 feature setting (1.30 vs 6.78), and class accuracy during interpolation (62% vs 52%). See Section G in the appendix for more details and ablations.

Low-dimensional subspaces In Figure 2 we illustrate two slices of a 5-dimensional subspace of the latent space, indexing high-dimensional images of sports cars. The subspace is defined using five images (one per dimension), formed using the COG method described in Section 2 to reweight the linear combinations of the corresponding projections. In Figure 7 we show the corresponding grid without the reweighting scheme. In the appendix (Section E) we also include more slices and examples; diffusion and flow matching models for images, and a point cloud diffusion model.

In this paper we propose COG, a generally applicable and simple scheme to ensure that linear combinations of latents follow the prespecified Gaussian distribution - critical for several classes of generative models - and demonstrate its effectiveness for interpolation and defining subspaces.

References

- Robert B Ash. *Information theory*. Courier Corporation, 2012.
- Angel X Chang, Thomas Funkhouser, Leonidas Guibas, Pat Hanrahan, Qixing Huang, Zimo Li, Silvio Savarese, Manolis Savva, Shuran Song, Hao Su, et al. Shapenet: An information-rich 3d model repository. *arXiv preprint arXiv:1512.03012*, 2015.
- Ricky TQ Chen, Yulia Rubanova, Jesse Bettencourt, and David K Duvenaud. Neural ordinary differential equations. *Advances in neural information processing systems*, 31, 2018.
- Jia Deng, Wei Dong, Richard Socher, Li-Jia Li, Kai Li, and Li Fei-Fei. Imagenet: A large-scale hierarchical image database. In *2009 IEEE conference on computer vision and pattern recognition*, pp. 248–255. Ieee, 2009.
- Patrick Esser, Sumith Kulal, Andreas Blattmann, Rahim Entezari, Jonas Müller, Harry Saini, Yam Levi, Dominik Lorenz, Axel Sauer, Frederic Boesel, et al. Scaling rectified flow transformers for high-resolution image synthesis. In *Forty-first International Conference on Machine Learning*, 2024.
- Ishaan Gulrajani, Faruk Ahmed, Martin Arjovsky, Vincent Dumoulin, and Aaron C Courville. Improved training of wasserstein gans. *Advances in neural information processing systems*, 30, 2017.
- René Haas, Inbar Huberman-Spiegelglas, Rotem Mulayoff, and Tomer Michaeli. Discovering interpretable directions in the semantic latent space of diffusion models. *arXiv preprint arXiv:2303.11073*, 3(6), 2023.
- Martin Heusel, Hubert Ramsauer, Thomas Unterthiner, Bernhard Nessler, and Sepp Hochreiter. Gans trained by a two time-scale update rule converge to a local nash equilibrium. *Advances in neural information processing systems*, 30, 2017.
- Jonathan Ho, Ajay Jain, and Pieter Abbeel. Denoising diffusion probabilistic models. *arXiv preprint arXiv:2006.11239*, 2020.
- Jonathan Ho, Tim Salimans, Alexey Gritsenko, William Chan, Mohammad Norouzi, and David J Fleet. Video diffusion models. *Advances in Neural Information Processing Systems*, 35:8633–8646, 2022.
- Zhifeng Kong, Wei Ping, Jiaji Huang, Kexin Zhao, and Bryan Catanzaro. Diffwave: A versatile diffusion model for audio synthesis. *arXiv preprint arXiv:2009.09761*, 2020.
- Mingi Kwon, Jaeseok Jeong, and Youngjung Uh. Diffusion models already have a semantic latent space. *arXiv preprint arXiv:2210.10960*, 2022.
- Yaron Lipman, Ricky TQ Chen, Heli Ben-Hamu, Maximilian Nickel, and Matt Le. Flow matching for generative modeling. *arXiv preprint arXiv:2210.02747*, 2022.
- Shitong Luo and Wei Hu. Diffusion probabilistic models for 3d point cloud generation. In *Proceedings of the IEEE/CVF Conference on Computer Vision and Pattern Recognition*, pp. 2837–2845, 2021.
- Eric Nalisnick, Akihiro Matsukawa, Yee Whye Teh, and Balaji Lakshminarayanan. Detecting out-of-distribution inputs to deep generative models using typicality. *arXiv preprint arXiv:1906.02994*, 2019.
- Dogyun Park, Sihyeon Kim, Sojin Lee, and Hyunwoo J Kim. Ddmi: Domain-agnostic latent diffusion models for synthesizing high-quality implicit neural representations. *arXiv preprint arXiv:2401.12517*, 2024.
- Robin Rombach, Andreas Blattmann, Dominik Lorenz, Patrick Esser, and Björn Ommer. High-resolution image synthesis with latent diffusion models. In *Proceedings of the IEEE/CVF conference on computer vision and pattern recognition*, pp. 10684–10695, 2022.

- Olaf Ronneberger, Philipp Fischer, and Thomas Brox. U-net: Convolutional networks for biomedical image segmentation. In *Medical image computing and computer-assisted intervention—MICCAI 2015: 18th international conference, Munich, Germany, October 5-9, 2015, proceedings, part III* 18, pp. 234–241. Springer, 2015.
- Dvir Samuel, Rami Ben-Ari, Nir Darshan, Haggai Maron, and Gal Chechik. Norm-guided latent space exploration for text-to-image generation. *Advances in Neural Information Processing Systems*, 36, 2024.
- Maximilian Seitzer. pytorch-fid: FID Score for PyTorch. <https://github.com/mseitzer/pytorch-fid>, August 2020. Version 0.3.0.
- Ken Shoemake. Animating rotation with quaternion curves. In *Proceedings of the 12th annual conference on Computer graphics and interactive techniques*, pp. 245–254, 1985.
- Jiaming Song, Chenlin Meng, and Stefano Ermon. Denoising diffusion implicit models. *arXiv preprint arXiv:2010.02502*, 2020a.
- Yang Song, Jascha Sohl-Dickstein, Diederik Kingma, Abhishek Kumar, Stefano Ermon, and Ben Poole. Score-based generative modeling through stochastic differential equations. *arXiv preprint arXiv:2011.13456*, 2020b.
- Michel Talagrand. Concentration of measure and isoperimetric inequalities in product spaces. *Publications Mathématiques de l’Institut des Hautes Etudes Scientifiques*, 81:73–205, 1995.
- Zhengzhong Tu, Hossein Talebi, Han Zhang, Feng Yang, Peyman Milanfar, Alan Bovik, and Yinxiao Li. Maxvit: Multi-axis vision transformer. In *European conference on computer vision*, pp. 459–479. Springer, 2022.
- Cédric Villani et al. *Optimal transport: old and new*, volume 338. Springer, 2009.
- Tom White. Sampling generative networks. *arXiv preprint arXiv:1609.04468*, 2016.

A Gaussian linear combinations

Lemma 1. Let \mathbf{y} be a linear combination of K i.i.d. random variables $\mathbf{x}^{(k)} \sim \mathcal{N}(\boldsymbol{\mu}, \boldsymbol{\Sigma})$, where \mathbf{y} is defined as

$$\mathbf{y} := \sum_{k=1}^K w_k \mathbf{x}^{(k)} = \mathbf{w}^T \mathbf{X},$$

with $w_k \in \mathbb{R}$, $\mathbf{y} \in \mathbb{R}^D$, $\mathbf{x}^{(k)} \in \mathbb{R}^D$, $\mathbf{w} = [w_1, w_2, \dots, w_K]$ and $\mathbf{X} = [\mathbf{x}^{(1)}, \mathbf{x}^{(2)}, \dots, \mathbf{x}^{(K)}]$. Then \mathbf{y} is a Gaussian random variable with the distribution

$$\mathbf{y} \sim \mathcal{N}(\alpha \boldsymbol{\mu}, \beta \boldsymbol{\Sigma}),$$

where

$$\alpha = \sum_{k=1}^K w_k \quad \text{and} \quad \beta = \sum_{k=1}^K w_k^2.$$

Proof. Given $\mathbf{x}^{(k)} \sim \mathcal{N}(\boldsymbol{\mu}, \boldsymbol{\Sigma})$, we know that each $\mathbf{x}^{(k)}$ has mean $\boldsymbol{\mu}$ and covariance matrix $\boldsymbol{\Sigma}$.

Define $\mathbf{y} = \mathbf{w}^T \mathbf{X} = \sum_{k=1}^K w_k \mathbf{x}^{(k)}$.

First, we calculate the mean of \mathbf{y} :

$$\mathbb{E}[\mathbf{y}] = \mathbb{E}\left[\sum_{k=1}^K w_k \mathbf{x}^{(k)}\right] = \sum_{k=1}^K w_k \mathbb{E}[\mathbf{x}^{(k)}] = \sum_{k=1}^K w_k \boldsymbol{\mu} = \left(\sum_{k=1}^K w_k\right) \boldsymbol{\mu} = \alpha \boldsymbol{\mu}.$$

Next, we calculate the covariance of \mathbf{y} :

$$\text{Cov}(\mathbf{y}) = \text{Cov} \left(\sum_{k=1}^K w_k \mathbf{x}^{(k)} \right) = \sum_{k=1}^K w_k^2 \text{Cov}(\mathbf{x}^{(k)}),$$

since the $\mathbf{x}^{(k)}$ are i.i.d. and thus $\text{Cov}(\mathbf{x}^{(i)}, \mathbf{x}^{(j)}) = 0$ for $i \neq j$.

Given that $\mathbf{x}^{(k)} \sim \mathcal{N}(\boldsymbol{\mu}, \boldsymbol{\Sigma})$, we have $\text{Cov}(\mathbf{x}^{(k)}) = \boldsymbol{\Sigma}$. Therefore,

$$\text{Cov}(\mathbf{y}) = \sum_{k=1}^K w_k^2 \boldsymbol{\Sigma} = \left(\sum_{k=1}^K w_k^2 \right) \boldsymbol{\Sigma} = \beta \boldsymbol{\Sigma}.$$

Hence, $\mathbf{y} \sim \mathcal{N}(\alpha \boldsymbol{\mu}, \beta \boldsymbol{\Sigma})$ with $\alpha = \sum_{k=1}^K w_k$ and $\beta = \sum_{k=1}^K w_k^2$.

□

Lemma 2. *Let \mathbf{z} be defined as*

$$\mathbf{z} = \mathbf{a} + \mathbf{B}\mathbf{y},$$

where

$$\mathbf{a} = \left(1 - \frac{\alpha}{\sqrt{\beta}} \right) \boldsymbol{\mu} \quad \text{and} \quad \mathbf{B} = \frac{1}{\sqrt{\beta}} \mathbf{I},$$

with $\mathbf{y} \sim \mathcal{N}(\alpha \boldsymbol{\mu}, \beta \boldsymbol{\Sigma})$. Then $\mathbf{z} \sim \mathcal{N}(\boldsymbol{\mu}, \boldsymbol{\Sigma})$.

Proof. Given $\mathbf{y} \sim \mathcal{N}(\alpha \boldsymbol{\mu}, \beta \boldsymbol{\Sigma})$, we need to show that $\mathbf{z} \sim \mathcal{N}(\boldsymbol{\mu}, \boldsymbol{\Sigma})$.

First, we calculate the mean of \mathbf{z} :

$$\mathbb{E}[\mathbf{z}] = \mathbb{E}[\mathbf{a} + \mathbf{B}\mathbf{y}] = \mathbf{a} + \mathbf{B}\mathbb{E}[\mathbf{y}] = \left(1 - \frac{\alpha}{\sqrt{\beta}} \right) \boldsymbol{\mu} + \frac{1}{\sqrt{\beta}} \alpha \boldsymbol{\mu} = \boldsymbol{\mu}.$$

Next, we calculate the covariance of \mathbf{z} :

$$\text{Cov}(\mathbf{z}) = \text{Cov}(\mathbf{a} + \mathbf{B}\mathbf{y}) = \mathbf{B}\text{Cov}(\mathbf{y})\mathbf{B}^T = \frac{1}{\sqrt{\beta}} \beta \boldsymbol{\Sigma} \frac{1}{\sqrt{\beta}} = \boldsymbol{\Sigma}.$$

Since \mathbf{z} has mean $\boldsymbol{\mu}$ and covariance $\boldsymbol{\Sigma}$, we conclude that

$$\mathbf{z} \sim \mathcal{N}(\boldsymbol{\mu}, \boldsymbol{\Sigma}).$$

□

B Spherical interpolants are approximately i.i.d. for high-dim unit Gaussians

Spherical linear interpolation (SLERP) Shoemake (1985) is defined as

$$\mathbf{y} = w_1 \mathbf{x}_1 + w_2 \mathbf{x}_2 \tag{4}$$

where

$$w_i := \frac{\sin v_i \theta}{\sin \theta}, \tag{5}$$

$v_i \in [0, 1]$ and $v_2 = 1 - v_1$ and $\cos \theta = \frac{\langle \mathbf{x}_1, \mathbf{x}_2 \rangle}{\|\mathbf{x}_1\| \|\mathbf{x}_2\|}$, where $\cos \theta$ is typically referred to as the *cosine similarity* of \mathbf{x}_1 and \mathbf{x}_2 .

As such, using Equation 2, we obtain

$$\alpha = \sum_{k=1}^K w_k = \frac{\sin v_1 \theta}{\sin \theta} + \frac{\sin v_2 \theta}{\sin \theta} \quad \text{and} \quad \beta = \frac{\sin^2 v_1 \theta}{\sin^2 \theta} + \frac{\sin^2 v_2 \theta}{\sin^2 \theta} \tag{6}$$

As discussed in Section 2, for a linear combination \mathbf{y} to be a random variable following distribution $\mathcal{N}(\boldsymbol{\mu}, \boldsymbol{\Sigma})$, given that \mathbf{x}_1 and \mathbf{x}_2 do, it must be true that $\alpha\boldsymbol{\mu} = \boldsymbol{\mu}$ and $\beta\boldsymbol{\Sigma} = \boldsymbol{\Sigma}$.

A common case is using unit Gaussian latents (as in e.g. the models Esser et al. (2024) and Rombach et al. (2022) used in this paper), i.e. where $\boldsymbol{\mu} = \mathbf{0}, \boldsymbol{\Sigma} = \mathbf{I}$. In this case it trivially follows that $\alpha\boldsymbol{\mu} = \boldsymbol{\mu}$ since $\alpha\mathbf{0} = \mathbf{0}$. We will now show that $\beta \approx 1$ in this special case.

Lemma 3. *Let*

$$\beta = \frac{\sin^2 v\theta}{\sin^2 \theta} + \frac{\sin^2(1-v)\theta}{\sin^2 \theta},$$

where $\cos \theta = \frac{\langle \mathbf{x}_1, \mathbf{x}_2 \rangle}{\|\mathbf{x}_1\| \|\mathbf{x}_2\|}$ and $\mathbf{x}_1, \mathbf{x}_2 \sim \mathcal{N}(\mathbf{0}, \mathbf{I})$. Then $\beta \approx 1$ for large D , $\forall v \in [0, 1]$.

Proof. Since $\mathbf{x}_1, \mathbf{x}_2 \sim \mathcal{N}(\mathbf{0}, \mathbf{I})$, each component x_{1j} and x_{2j} for $j = 1, \dots, D$ are independent standard normal random variables. The inner product $\langle \mathbf{x}_1, \mathbf{x}_2 \rangle$ is given by:

$$\langle \mathbf{x}_1, \mathbf{x}_2 \rangle = \sum_{j=1}^D x_{1j} x_{2j}.$$

The product $x_{1j} x_{2j}$ follows a distribution known as the standard normal product distribution. For large D , the sum of these products is approximately normal due to the Central Limit Theorem (CLT), with:

$$\langle \mathbf{x}_1, \mathbf{x}_2 \rangle \sim \mathcal{N}(0, D).$$

Next, consider the norms $\|\mathbf{x}_1\|$ and $\|\mathbf{x}_2\|$. Each $\|\mathbf{x}_i\|^2 = \sum_{j=1}^D x_{ij}^2$ is a chi-squared random variable with D degrees of freedom. For large D , by the central limit theorem, $\|\mathbf{x}_i\|^2 \sim \mathcal{N}(D, 2D)$, and therefore $\|\mathbf{x}_i\|$ is approximately \sqrt{D} .

Thus, for large D ,

$$\cos(\theta) = \frac{\langle \mathbf{x}_1, \mathbf{x}_2 \rangle}{\|\mathbf{x}_1\| \|\mathbf{x}_2\|} \approx \frac{\mathcal{N}(0, D)}{\sqrt{D} \cdot \sqrt{D}} = \frac{\mathcal{N}(0, D)}{D} = \mathcal{N}\left(0, \frac{1}{D}\right).$$

Thus, $\theta \approx \pi/2$, which implies $\sin(\theta) \approx 1$. Therefore:

$$\beta = \frac{\sin^2(v\theta)}{\sin^2 \theta} + \frac{\sin^2((1-v)\theta)}{\sin^2 \theta} \approx \sin^2(v\theta) + \sin^2((1-v)\theta).$$

Using the identity $\sin^2(a) + \sin^2(b) = 1 - \cos^2(a-b)$,

$$\beta \approx 1 - \cos^2(v\theta - (1-v)\theta) = 1 - \cos^2(\theta)$$

Given $v \in [0, 1]$ and $\theta \approx \pi/2$ for large D , the argument of \cos remains small, leading to $\cos(\cdot) \approx 0$. Hence,

$$\beta \approx 1.$$

Therefore, for large D , $\beta \approx 1$.

□

Empirical verification To confirm that this approximation is good for numbers of dimensions D seen in popular models using unit Gaussian latents, we estimate the confidence interval of β using 10k samples of \mathbf{x}_1 and \mathbf{x}_2 , respectively, where $\mathbf{x}_i \sim \mathcal{N}(\mathbf{0}, \mathbf{I})$. For Stable Diffusion 3 Esser et al. (2024), a flow-matching model with $D = 147456$, the estimated 99% confidence interval of β is $[0.9934, 1.0067]$. For Stable Diffusion 2.1 Rombach et al. (2022), a diffusion model with $D = 36864$, the estimated 99% confidence interval of β is $[0.9868, 1.014]$.

C Linear combination weights of subspace projections

Lemma 4. Let $U \in \mathbb{R}^{D \times K}$ be a semi-orthonormal matrix. For a given point $x \in \mathbb{R}^D$, the subspace projection is $s(x) = UU^T x$. The weights $w \in \mathbb{R}^K$ such that $s(x)$ is a linear combination of x_1, x_2, \dots, x_K (columns of $A = [x_1, x_2, \dots, x_K] \in \mathbb{R}^{D \times K}$) can be expressed as $w = A_{\dagger} s(x)$, where A_{\dagger} is the Moore-Penrose inverse of A .

Proof. The subspace projection $s(x)$ of $x \in \mathbb{R}^D$ is defined as:

$$s(x) = UU^T x.$$

We aim to express $s(x)$ as a linear combination of the columns of $A = [x_1, x_2, \dots, x_K] \in \mathbb{R}^{D \times K}$. That is, we seek $w \in \mathbb{R}^K$ such that:

$$s(x) = Aw.$$

By definition, the Moore-Penrose inverse A_{\dagger} of A satisfies the following properties:

1. $AA_{\dagger}A = A$
2. $A_{\dagger}AA_{\dagger} = A_{\dagger}$
3. $(AA_{\dagger})^T = AA_{\dagger}$
4. $(A_{\dagger}A)^T = A_{\dagger}A$

Since $s(x)$ is in the subspace spanned by the columns of A , there exists a w such that:

$$s(x) = Aw.$$

Consider a $w' \in \mathbb{R}^K$ constructed using the Moore-Penrose inverse A_{\dagger} :

$$w' = A_{\dagger} s(x).$$

We now verify that this w' satisfies the required equation. Substituting back

$$Aw' = A(A_{\dagger} s(x))$$

and using the property of the Moore-Penrose inverse $AA_{\dagger}A = A$, we get:

$$AA_{\dagger} s(x) = s(x).$$

Thus:

$$Aw' = s(x),$$

which shows that $w' = A_{\dagger} s(x)$ is indeed the correct expression for the weights.

From uniqueness of w for a given set of columns x_1, x_2, \dots, x_K (see Lemma 5), we have proven that the weights w for a given point in the subspace $s(x)$ are given by:

$$w = A_{\dagger} s(x).$$

□

Lemma 5. The weights $w \in \mathbb{R}^K$ such that $s(x)$ is a linear combination of x_1, x_2, \dots, x_K (columns of $A = [x_1, x_2, \dots, x_K] \in \mathbb{R}^{D \times K}$) are unique.

Proof. Suppose there exist two different weight vectors w_1 and w_2 such that both satisfy the equation:

$$s(x) = Aw_1 = Aw_2.$$

Then, subtracting these two equations gives:

$$Aw_1 - Aw_2 = 0.$$

This simplifies to:

$$\mathbf{A}(\mathbf{w}_1 - \mathbf{w}_2) = \mathbf{0}.$$

Let $\mathbf{v} = \mathbf{w}_1 - \mathbf{w}_2$. Then:

$$\mathbf{A}\mathbf{v} = \mathbf{0}.$$

Since $\mathbf{v} \in \mathbb{R}^K$, this equation implies that \mathbf{v} lies in the null space of \mathbf{A} . However, the assumption that \mathbf{A} has full column rank (since \mathbf{A} is used to represent a linear combination for $s(\mathbf{x})$) implies that \mathbf{A} has no non-zero vector in its null space, i.e., $\mathbf{A}\mathbf{v} = \mathbf{0}$ only when $\mathbf{v} = \mathbf{0}$.

Therefore:

$$\mathbf{v} = \mathbf{0} \implies \mathbf{w}_1 = \mathbf{w}_2.$$

This shows that the weights \mathbf{w} are unique, and there cannot be two distinct sets of weights \mathbf{w}_1 and \mathbf{w}_2 that satisfy the equation $s(\mathbf{x}) = \mathbf{A}\mathbf{w}$.

Hence, we conclude that the weights \mathbf{w} such that $s(\mathbf{x})$ is a linear combination of $\mathbf{x}_1, \mathbf{x}_2, \dots, \mathbf{x}_K$ are unique. \square

D Interpolation and centroid determination setup details

Baselines For the application of interpolation, we compare to linear interpolation (LERP), spherical linear interpolation (SLERP), and Norm-Aware Optimization (NAO) Samuel et al. (2024), a recent approach which considers the norm of the noise vectors. In contrast to the other approaches which only involve analytical expressions, NAO involves a numerical optimization scheme based on a discretization of a line integral. For the application of centroid determination we compare to NAO, the Euclidean centroid $\bar{\mathbf{x}} = \frac{1}{K} \sum_{k=1}^K \mathbf{x}_k$, and two transformations of the Euclidean centroid; "standardized Euclidean", where $\bar{\mathbf{x}}$ is subsequently standardized to have mean zero and unit variance, and "mode norm Euclidean", where $\bar{\mathbf{x}}$ is rescaled to have the norm equal to the (square root of the) mode of $\chi^2(D)$, the chi-squared distribution with D degrees of freedom, which is the maximum likelihood norm given that \mathbf{x} has been generated from a unit Gaussian with D dimensions.

Evaluation sets We closely follow the evaluation protocol in Samuel et al. (2024), where we base the experiments on Stable Diffusion 2 Rombach et al. (2022) and inversions of random images from ImageNet1k Deng et al. (2009). We (uniformly) randomly select 50 classes, each from which we randomly select 50 unique images, and find their corresponding latents through DDIM inversion Song et al. (2020a) using the class name as prompt. We note that the DDIM inversion can be sensitive to the number of steps, especially in obtaining the correct norm. Therefore, we made sure to use a sufficient number of steps for the inversion (we used 400 steps), which we then matched for the generation; see Figure 12 for an illustration of the importance of using a sufficient number of steps. We used the guidance scale 1.0 (i.e. no guidance) for the inversion, which was then matched during generation. Note that using no guidance is important both for accurate inversion as well as to not introduce a factor (the dynamics of prompt guidance) which would be specific to the Stable Diffusion 2.1 model.

For the interpolation setup we randomly (without replacement) pair the 50 images per class into 25 pairs, forming 1250 image pairs in total. In between the ends of each respective pair, each method then is to produce three interpolation points (and images). For the NAO method, which needs additional interpolation points to approximate the line integral, we used 11 interpolation points and selected three points from these at uniform (index) distance, similar to in Samuel et al. (2024).

For the centroid determination setup we for each class form 10 3-groups, 10 5-groups, 4 10-groups and 1 25-group, sampled without replacement per group¹, each method then to form 25 centroids per class (for a total of 1250 centroids per method). Similarly to each the interpolation setup, for NAO we used 11 interpolations points per path, which for their centroid determination method entails K paths per centroid.

¹But with replacement across groups, i.e. the groups are sampled independently from the same collection of images.

Evaluation We, as in Samuel et al. (2024), assess the methods quantitatively based on visual quality and preservation of semantics, using FID scores and class prediction accuracy, respectively.

The FID scores are computed using the pytorch-fid library Seitzer (2020), using all evaluation images produced per method for the interpolation and centroid determination respectively, to maximize the FID score estimation accuracy.

For the classification accuracy, we used a pre-trained classifier, the MaxViT image classification model Tu et al. (2022) as in Samuel et al. (2024), which achieves a top-1 of 88.53% and 98.64% top-5 accuracy on the test-set of ImageNet.

See results in Section G.

E Additional qualitative results

See Figure 3 for additional slices of the sports car subspace shown in Figure 2.

See Figure 4 for a subspace of the latents of point clouds from the diffusion model in Park et al. (2024). The latents in this model generates modality agnostic representations (which they use for images, video, 3D shapes, and textures) which in turn is used to generate a mesh which is subsequently converted into a point cloud. Note that we can apply COG to any generative model with Gaussian latents, and we were able to define the subspace without any further assumptions or modifications to their code.

See Figure 5 for an additional subspace example using the flow matching model Stable Diffusion 3 (SD3), this time of rocking chairs. The only difference in setup to the sports car examples in Figure 3 and Figure 2 is the prompt used for the generation in the SD3 model and the selection of latents to form basis vectors.

See Figure 6 for an interpolation example.

See Figure 7 for a demonstration of subspaces of latents *without* the COG scheme introduced in Equation 3, using a diffusion model Rombach et al. (2022) and a flow matching model Esser et al. (2024), respectively. The setup is identical (with the same original latents) as in Figure 8 and Figure 2, respectively, except without applying the proposed (COG) transformation.

See Figure 8 and Figure 9 for Stable Diffusion 2.1 (SD2.1) versions of the Stable Diffusion 3 (SD3) examples in Figure 2 and Figure 5, with an otherwise identical setup including the prompts. Just like in the SD3 examples COG defines working subspaces. However, as expected since SD2.1 is an older model than SD3, the visual quality of the generations is better using SD3.

In the examples above the SD2.1 and SD3 models are provided with a text prompt during the generation. See Figure 10 for an example where the original latents ($\{x_i\}$) were obtained using DDIM inversion (from images) without a prompt (and guidance scale 1.0, i.e. no guidance), allowing generation without a prompt. This allows us to also interpolate without conditioning on a prompt. We note that, as expected without a prompt, the intermediates are not necessarily related to the end points (the original images) but still realistic images are obtained as expected (except for using linear interpolation, see discussion in Section 2) and the interpolations yield smooth gradual changes.

F High likelihood vectors can be very atypical

The distribution of the latent variable x in a diffusion or flow matching model is (with few exceptions) Gaussian $\mathcal{N}(u, \Sigma)$, and the covariance matrix Σ is typically diagonal.

A possibly common misconception is that the density function $\mathcal{N}(x; u, \Sigma)$ of the distribution is a proxy to indicate how well a particular vector x is supported by the model. Where, for example, one would expect vectors with very high likelihood, such as the mode, to be well supported. However, a vector merely being likely under the distribution does not imply it is well characterised as a sample from it (discussed below). The model has exclusively been trained on samples from the distribution (at the first timestep of the generative process), and if the vector lack the characteristics of a typical sample (expected to be observed during training during any feasible length of time) it may fall outside the support of the trained neural network.



Figure 3: **Additional slices of a sports car subspace.** The latents x_1, \dots, x_5 (corresponding to images) are converted into basis vectors and used to define a 5-dimensional subspace. The grids show generations from uniform grid points in the subspace coordinate system, where the left and right grids are for the dimensions $\{1, 2\}$ and $\{3, 4\}$, respectively, centered around the coordinate for x_1 . Each coordinate in the subspace correspond to a linear combination of the basis vectors. The flow-matching model Stable Diffusion 3 Esser et al. (2024) is used in this example. See Figure 2 for two other slices of the space.

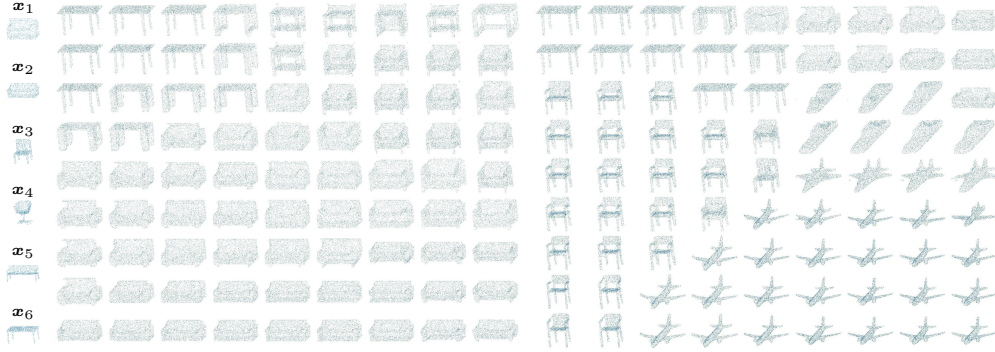


Figure 4: **Point cloud subspace example.** The latents x_1, \dots, x_6 (which via generation corresponds to neural representations, see the DDMI paper) are converted into basis vectors and used to define a 6-dimensional subspace. The grids show generations from uniform grid points in the subspace coordinate system, where the left and right grids show dimensions $\{1, 2\}$ centered around the coordinate for x_1 and x_3 , respectively. Each coordinate in the subspace correspond to a linear combination of the basis vectors. The diffusion model DDMI Park et al. (2024) is used in this example, and has been trained on the 3D CAD model dataset ShapeNet Chang et al. (2015).

The density of a Gaussian with a diagonal covariance matrix can equivalently be viewed as a product of independent univariate densities. The mismatch between model support and likelihood occurs due to the quickly shrinking concentration of points near the centre (or close to μ , where the likelihood is highest) as the dimensionality is increased Talagrand (1995); Ash (2012); Nalisnick et al. (2019); and the dimensionality is in general very high for these models, e.g. $D = 147456$ in Stable Diffusion 3 Esser et al. (2024) and $D = 36864$ in Stable Diffusion 2.1 Rombach et al. (2022).

As a case in point, discussed in e.g. Nalisnick et al. (2019); Samuel et al. (2024), is that the squared norm $\|x\|^2$ of a unit Gaussian vector $x \sim \mathcal{N}(\mathbf{0}, \mathbf{I})$ follows the chi-squared distribution $\chi^2(D)$ with D degrees of freedom, which is concentrated around D . In the case of $D = 36864$ as above, this means e.g. that (given that $x \sim \mathcal{N}(\mathbf{0}, \mathbf{I})$) the probability of observing a norm which is smaller than 186.21 (or larger than 197.83) is only $1e^{-16}$, and the probability of observing a norm anywhere near the norm of 0 (which is 0) is virtually zero. In Figure 11 we illustrate for a flow matching and

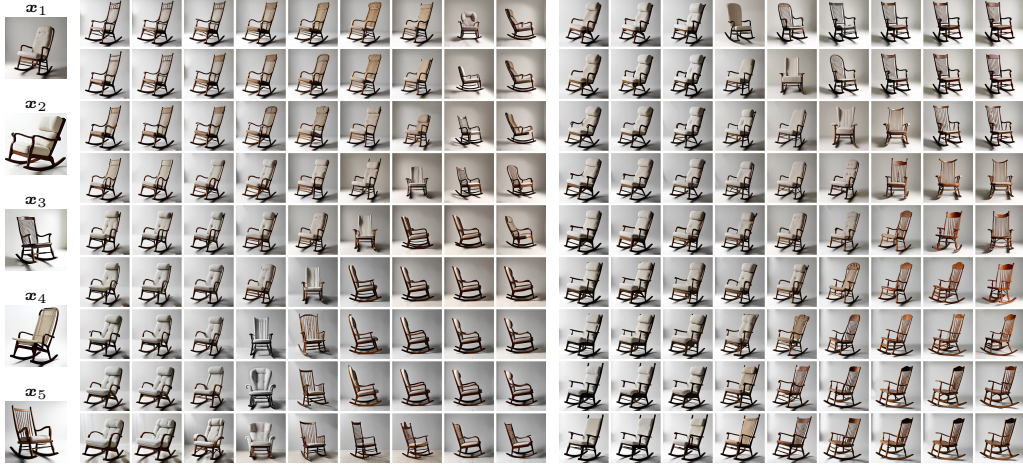


Figure 5: **Low-dimensional subspaces.** The latents x_1, \dots, x_5 (corresponding to images) are converted into basis vectors and used to define a 5-dimensional subspace. The grids show generations from uniform grid points in the subspace coordinate system, where the left and right grids are for the dimensions $\{1, 2\}$ and $\{3, 4\}$, respectively, centered around the coordinate for x_1 . Each coordinate in the subspace correspond to a linear combination of the basis vectors. The flow-matching model Stable Diffusion 3 Esser et al. (2024) is used in this example.

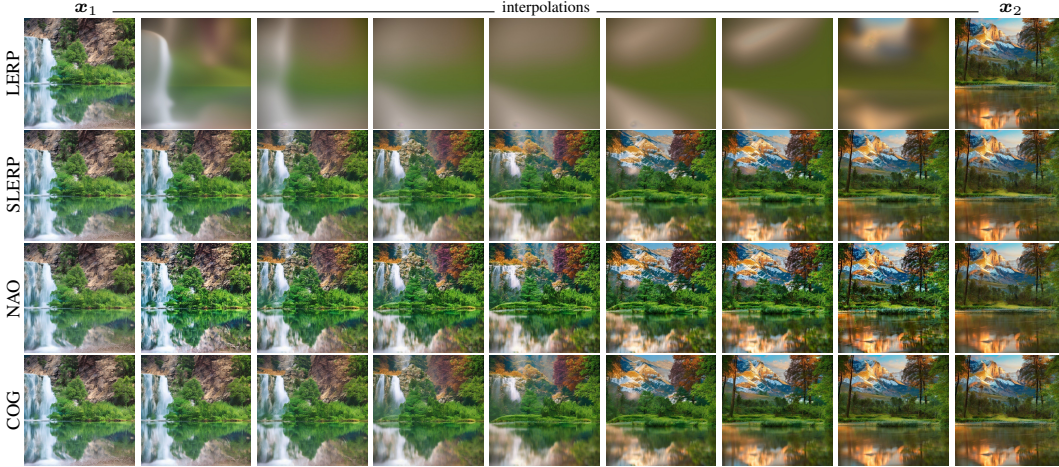


Figure 6: **Interpolation.** Shown are generations from equidistant interpolations of latents x_1 and x_2 (in $v \in [0, 1]$) using the respective method. The diffusion model Stable Diffusion 2.1 Rombach et al. (2022) is used in this example.

diffusion model, respectively, that; (1) the mode has a likelihood vastly larger than the likelihood of any sample, and (2) the mode (when treated as x and used for generation) does not yield realistic generations; i.e. is not similar to the data the network has been trained on and does not adhere to the prompt. In the case of the flow matching model the mode does yield a generated image of the subject in the prompt, although without detail.

However, it is not the lack of typicality of the *likelihood value* that makes the mode **0** poorly characterised as a sample from the distribution. There exists many vectors with a "typical" likelihood which still is very atypical (and which do not produce valid generations); e.g. a *constant vector* appropriately scaled to have the same likelihood as an actual sample. We illustrate this by example in Figure 11. Moreover, we also illustrate that a vector may have a typical norm, as well as the most likely norm, and still not be a sufficiently sample-like to produce valid generations.

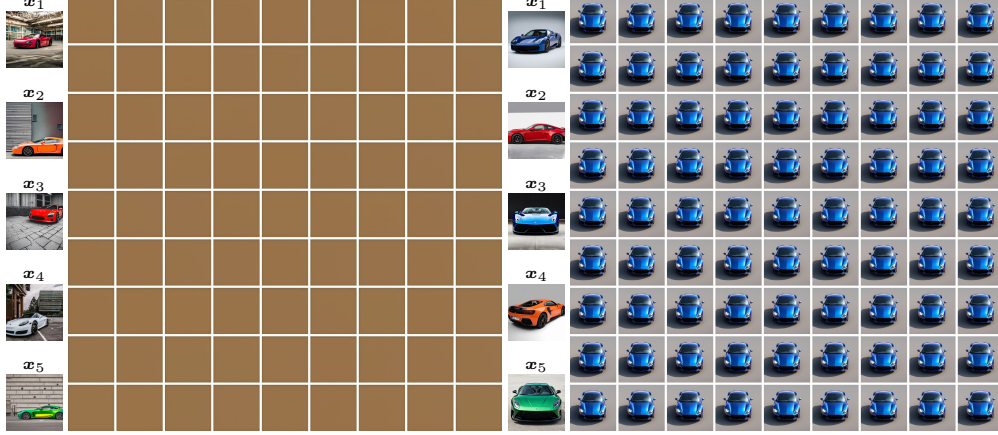


Figure 7: **Without COG reweighting.** The setup here is exactly the same as in Figure 8 and Figure 2, respectively, except without the proposed (COG) transformation (see Equation 3). The prompt used is "A high-quality photo of a parked, colored sports car taken with a DLSR camera with a 45.7MP sensor. The entire sports car is visible in the centre of the image. The background is simple and uncluttered to keep the focus on the sports car, with natural lighting enhancing its features.". We note that the diffusion model does not produce images of a car without the transformation, and neither model produce anything else than visually the same image for all coordinates.



Figure 8: **Low-dimensional subspaces.** The latents x_1, \dots, x_5 (corresponding to images) are converted into basis vectors and used to define a 5-dimensional subspace. The grids show generations from uniform grid points in the subspace coordinate system, where the left and right grids are for the dimensions $\{1, 3\}$ and $\{2, 4\}$, respectively, centered around the coordinate for x_1 . Each coordinate in the subspace correspond to a linear combination of the basis vectors. The diffusion model Stable Diffusion 2.1 Rombach et al. (2022) is used in this example.

G Additional quantitative results and analysis

In Table 1 we show that our method outperforms the baselines in terms of FID scores and accuracy, as calculated using a pre-trained classifier following the evaluation methodology of Samuel et al. (2024). Surprisingly, NAO did not perform as well as spherical interpolation and several other baselines, despite that we used their implementation and it was outperforming these methods in Samuel et al. (2024). We note that one discrepancy is that we report FID scores using the standard number of features (2048), while in their paper they are using fewer (64), which in Seitzer (2020) is not recommended since it does not necessarily correlate with visual quality. In Table 2 we report the results all settings of features. We note that, in our setup, the baselines performs substantially better than reported in their setup - including NAO in terms of FID scores using the 64 feature setting

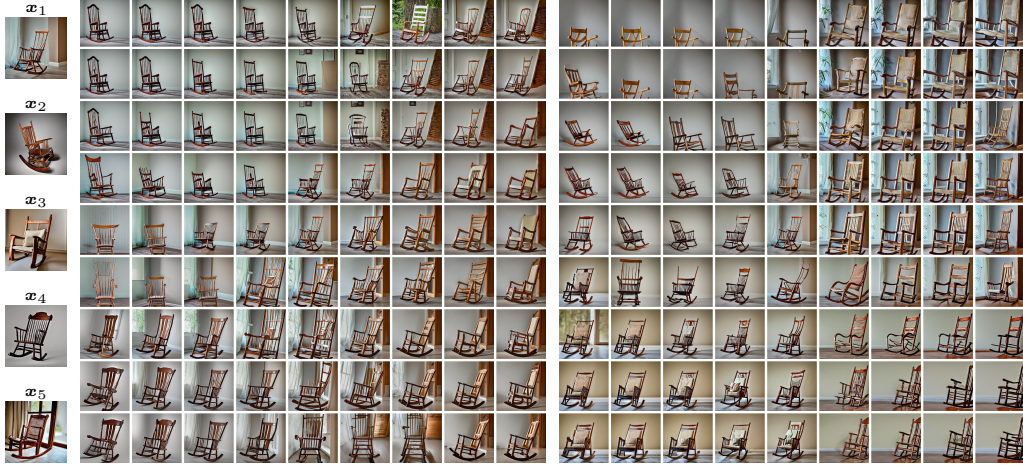


Figure 9: **Low-dimensional subspaces.** The latents x_1, \dots, x_5 (corresponding to images) are converted into basis vectors and used to define a 5-dimensional subspace. The grids show generations from uniform grid points in the subspace coordinate system, where the left and right grids are for the dimensions $\{1, 3\}$ and $\{2, 4\}$, respectively, centered around the coordinate for x_1 . Each coordinate in the subspace correspond to a linear combination of the basis vectors. The diffusion model Stable Diffusion 2.1 Rombach et al. (2022) is used in this example.

(1.30 vs 6.78), and class accuracy during interpolation; NAO got 62% in our and 52% in their setup. However, the accuracy they obtained for NAO in their setup was higher than in our setup; 67% vs 44%, which we study below.

The number of DDIM inversion steps used for the ImageNet images is not reported in the NAO setup Samuel et al. (2024), but if we use *1 step* instead of 400 (400 is what we use in all our experiments) the class preserving accuracy of NAO for centroid determination, shown in Table 3, resemble theirs more, yielding 58%. As we illustrate in Figure 12, a sufficient the number of inversion steps is critical to acquire latents which not only reconstructs the original image but which can be successfully interpolated. We hypothesise that a much lower setting of DDIM inversions steps were used in their setup than in ours, which would be consistent with their norm-correcting optimization method having a large effect, making otherwise blurry/superimposed images intelligible for the classification model.

Interpolation						
Method	Accuracy	FID 64	FID 192	FID 768	FID 2048	Time
LERP	3.92%	63.4	278	2.18	199	$6e^{-3}s$
SLERP	64.6%	2.28	4.95	0.173	42.6	$9e^{-3}s$
NAO	62.1%	1.30	4.11	0.195	46.0	30s
COG (ours)	67.4%	1.72	3.62	0.156	38.9	$6e^{-3}s$
Centroid determination						
Method	Accuracy	FID 64	FID 192	FID 768	FID 2048	Time
Euclidean	0.286%	67.7	317	3.68	310	$4e^{-4}s$
Standardized Euclidean	44.6%	5.92	21.0	0.423	88.8	$1e^{-3}s$
Mode norm Euclidean	44.6%	6.91	21.6	0.455	88.4	$1e^{-3}s$
NAO	44.0%	4.16	15.6	0.466	93.0	90s
COG (ours)	46.3%	9.38	25.5	0.455	87.7	$6e^{-4}s$

Table 2: Full table with class accuracy and FID scores using each setting in Seitzer (2020). Note that FID 64, 192, and 768 is not recommended by Seitzer (2020), as it does not necessarily correlate with visual quality. FID 2048 is based on the final features of InceptionV3 (as in Heusel et al. (2017)), while FID 64, 192 and 768 are based on earlier layers; FID 64 being the first layer.

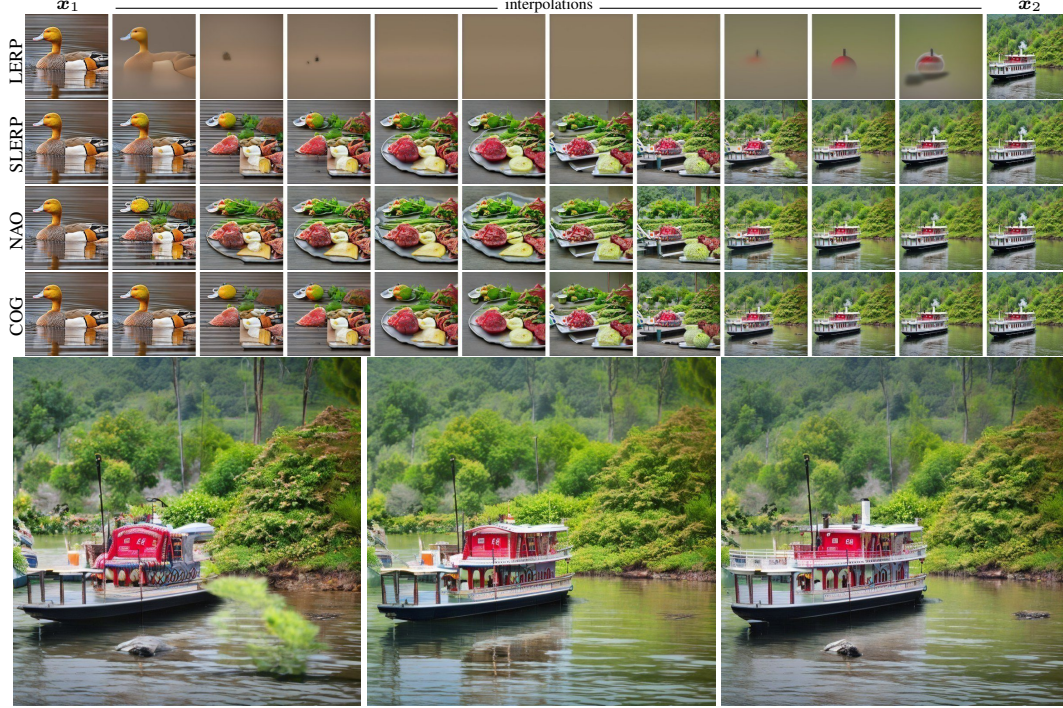


Figure 10: **Interpolation during unconditional generation.** Shown are generations from equidistant interpolations of latents x_1 and x_2 using the respective method. The latents x_1 and x_2 were obtained from DDIM inversion Song et al. (2020a) with an empty prompt, and all generations in this example are then carried out with an empty prompt. The larger images show interpolation index 8 for SLERP, NAO and COG, respectively. The diffusion model Stable Diffusion 2.1 Rombach et al. (2022) is used in this example.

Centroid determination of invalid latents						
Method	Accuracy	FID 64	FID 192	FID 768	FID 2048	Time
Euclidean	42.3%	25.7	59.3	1.23	170	$4e^{-4}$ s
Standardized Euclidean	46.6%	3.35	16.6	1.23	175	$1e^{-3}$ s
Mode norm Euclidean	50.6%	2.08	8.74	1.19	173	$1e^{-3}$ s
NAO	57.7%	3.77	13.3	1.05	150	90s
COG (ours)	48.6%	2.96	12.5	1.22	171	$6e^{-4}$ s

Table 3: Centroid determination results if we would use a *single step* for the DDIM inversion (not recommended). This results in latents which do *not* follow the correct distribution $\mathcal{N}(\mu, \Sigma)$ and which, despite reconstructing the original image exactly (if generating also using a single step), cannot be used successfully for interpolation; see Figure 12 for an example of the result of interpolation inversions using a varying number of steps. As illustrated in the figure, interpolations of latents obtained through a single step of DDIM inversion merely results in the two images being superimposed. Note that the class accuracy is much higher for all methods on such superimposed images, compared to using DDIM inversion settings which allow for realistic interpolations (see Table 2). Moreover, the FID scores set to use fewer features are *lower* for these superimposed images, while with recommended setting for FID scores (with 2048 features) they are higher (i.e. worse), as one would expect by visual inspection. The NAO method, initialized by the latent yielding the superimposed image, then optimises the latent yielding a norm close to norms of typical latents, which as indicated in the table leads to better "class preservation accuracy". However, the images produced with this setting are clearly unusable as they do not look like real images.

H Additional ImageNet interpolations and centroids

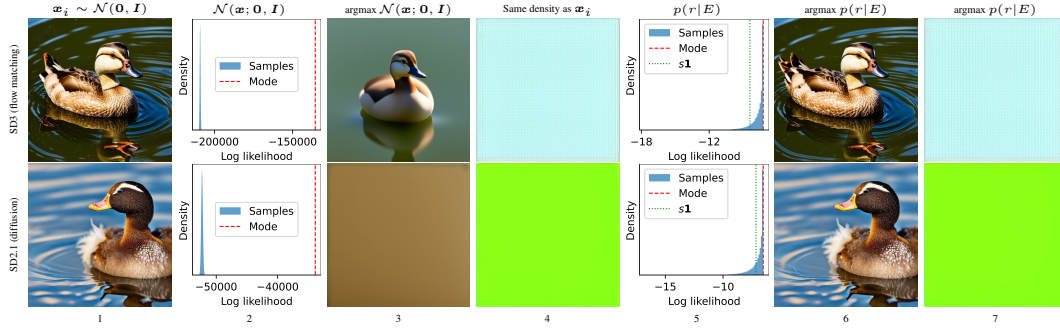


Figure 11: Likelihood does not equate to model support. In column (1) the generated image of a random sample is shown using a flow matching Esser et al. (2024) and a diffusion model Rombach et al. (2022), respectively, used with the prompt "A high-quality photo of a duck in a pond. The image is captured with a professional DSLR camera, ensuring incredible detail and clarity. The water is glittering in the sun and the duck is prominently featured in the center of the frame, showcasing its soft, fluffy feathers and bright, curious eyes". In column (2) the distribution of log likelihoods $\log \mathcal{N}(\mathbf{x}; \mathbf{0}, \mathbf{I})$, $\mathbf{x} \sim \mathcal{N}(\mathbf{0}, \mathbf{I})$ is shown, estimated using 100k samples, together with the log likelihood of the mode of the pre-specified distribution for the models, the zero vector $\mathbf{0}$. We note that the mode constitute an extreme outlier, with vastly higher likelihood than any sample. In column (3) we show the generation obtained from using the mode ($\mathbf{0}$) as the latent. In column (4) we show the generated images for the vector $s\mathbf{1}$, where s is set to have the *identical* likelihood value to the sample shown in column (1), to illustrate that the likelihood is not a proxy for model support. In column (5) the likelihood of the norm $r = \|\mathbf{x}\|$ is shown, for the same 100k samples as well as the mode $\text{argmax}_p(r|E)$, respectively. Note that in contrast to for the Gaussian likelihood $\mathcal{N}(\mathbf{x}; \mathbf{0}, \mathbf{I})$, this mode is not an "outlier" under its own distribution (since it does not constitute an independent product distribution in high dimensions). However, the mode reflects only one aspect of the sample; in column (6) and (7), we illustrate a valid and invalid generated image, respectively, both having a latent with the maximum likelihood norm. The first such latent is a rescaled version of \mathbf{x}_i , and the second is a rescaled version of the constant vector.

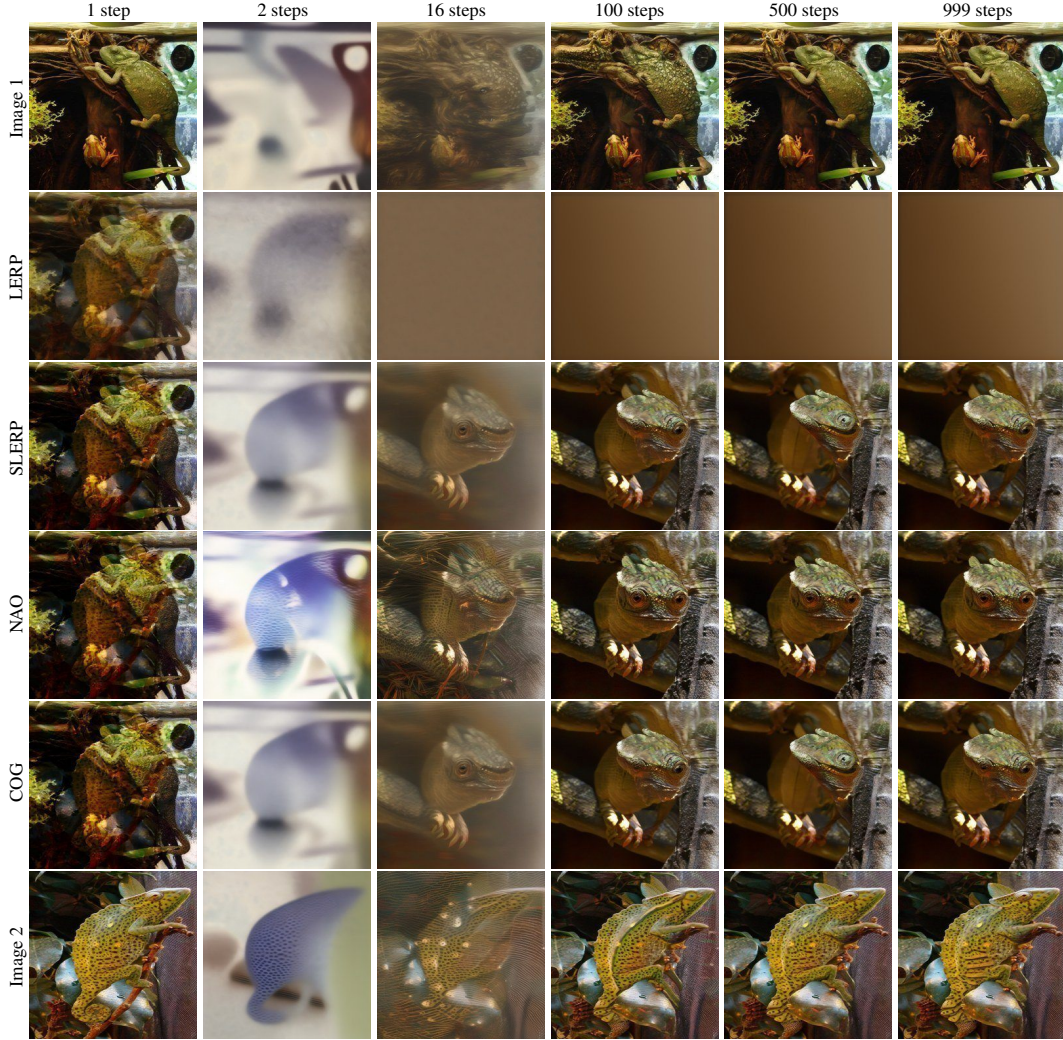


Figure 12: **Accurate DDIM inversions are critical for interpolation.** Shown is the interpolation (center) of Image 1 and Image 2 using each respective method, after a varying number of budgets of DDIM inversion steps Song et al. (2020a). For each budget setting, the inversion was run from the beginning. We note that although a single step of DDIM inversion yields latents which perfectly reconstructs the original image such latents do not lead to realistic images, but merely visual "superpositions" of the images being interpolated. In our quantitative and qualitative experiments we used 400 inversion steps, which we found to be sufficient for the latents to converge.

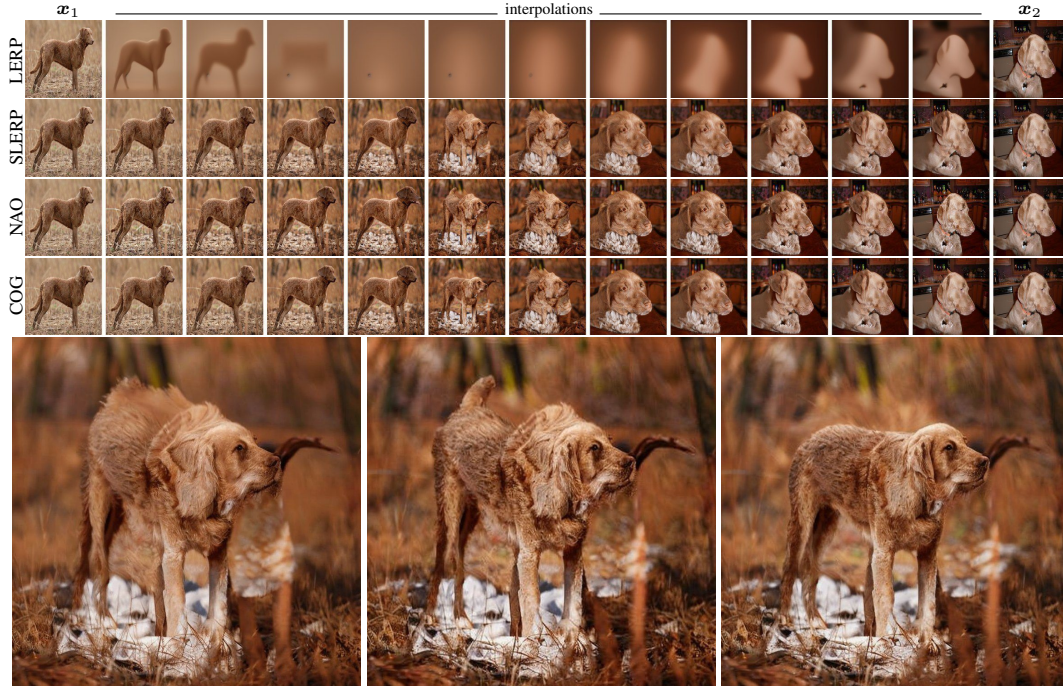


Figure 13: **Interpolation.** Shown are generations from equidistant interpolations of latents x_1 and x_2 using the respective method. The latents x_1 and x_2 were obtained from DDIM inversion Song et al. (2020a) of two random image examples from one of the randomly selected ImageNet classes ("Chesapeake Bay retriever") described in Section 3. The larger images show interpolation index 6 for SLERP, NAO and COG, respectively. The diffusion model Stable Diffusion 2.1 Rombach et al. (2022) is used in this example.

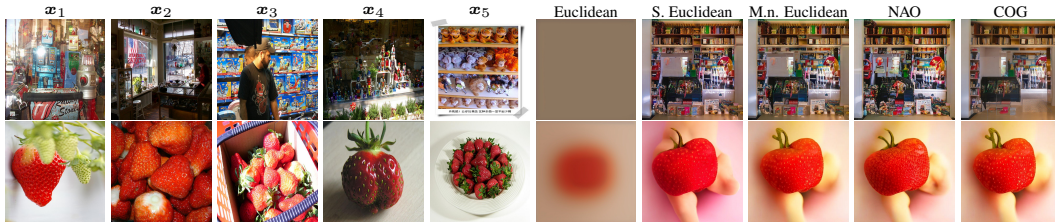


Figure 14: **ImageNet centroid determination.** The centroid of the latents x_1 , x_2 , x_3 as determined using the different methods, with the result shown in the respective (right-most) plot. The diffusion model Stable Diffusion 2.1 Rombach et al. (2022) is used in this example.

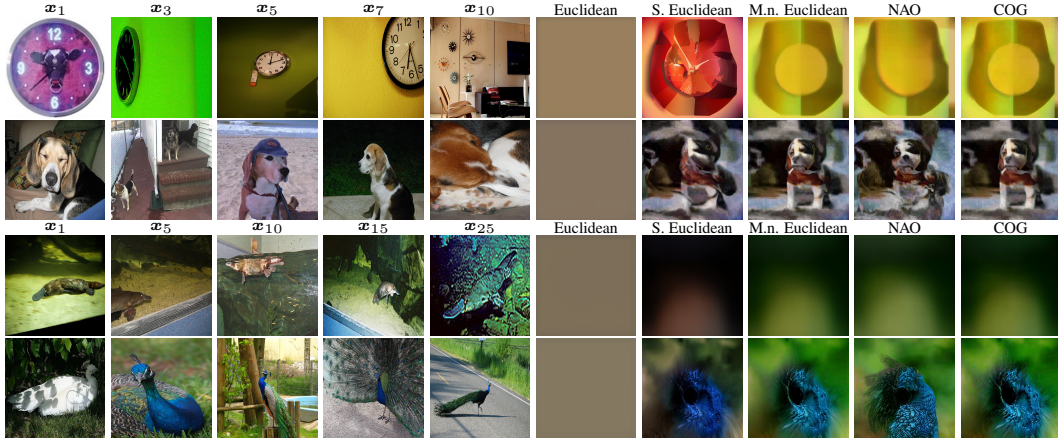


Figure 15: **Centroid determination of many latents.** The centroid of the latents as determined using the different methods, with the result shown in the respective (right-most) plot. Ten and 25 latents are used in the first two and second two examples (rows), respectively, and the plots show a subset of these in the left-most plots. We noted during centroid determination of many latents (such as 10 and 25) that the centroids were often unsatisfactory using all methods; blurry, distorted etc. For applications needing to find meaningful centroids of a large number of latents, future work is needed. The diffusion model Stable Diffusion 2.1 Rombach et al. (2022) is used in this example.